THE JOURNAL OF
PHYSICAL CHEMISTRY
LETTERS
A JOURNAL OF THE AMERICAN CHEMICAL SOCIETY

Absolute Quantification of sp^3 Defects in Semiconducting Single-Wall Carbon Nanotubes by Raman Spectroscopy

Finn L. Sebastian, Nicolas F. Zorn, Simon Settele, Sebastian Lindenthal, Felix J. Berger, Christoph Bendel, Han Li, Benjamin S. Flavel, and Jana Zaumseil*

Cite This: *J. Phys. Chem. Lett.* 2022, 13, 3542−3548 Read Online

ACCESS | Metrics & More | Article Recommendations | Supporting Information

ABSTRACT: The functionalization of semiconducting single-wall carbon nanotubes (SWCNTs) with luminescent sp^3 defects creates red-shifted emission features in the near-infrared and boosts their photoluminescence quantum yields (PLQYs). While multiple synthetic routes for the selective introduction of sp^3 defects have been developed, a convenient metric to precisely quantify the number of defects on a SWCNT lattice is not available. Here, we present a direct and simple quantification protocol based on a linear correlation of the integrated Raman D/G$^+$ signal ratios and defect densities as extracted from PLQY measurements. Corroborated by a statistical analysis of single-nanotube emission spectra at cryogenic temperature, this method enables the quantitative evaluation of sp^3 defect densities in (6,5) SWCNTs with an error of ±3 defects per micrometer and the determination of oscillator strengths for different defect types. The developed protocol requires only standard Raman spectroscopy and is independent of the defect configuration, dispersion solvent, and nanotube length.

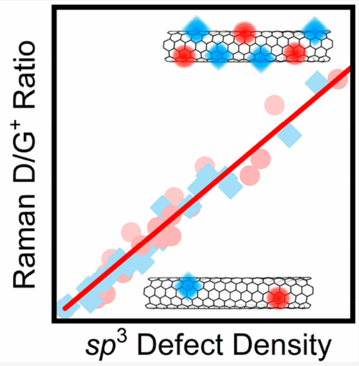

The chemical modification of semiconducting single-wall carbon nanotubes (SWCNTs) is a versatile tool to tune their properties for various applications such as quantum-light sources,[1−3] sensing, or bioimaging.[4−7] In particular, covalent functionalization of SWCNTs with luminescent sp^3 defects (also referred to as organic color centers) creates red-shifted emissive states in the near-infrared (NIR).[8−12] These states exhibit deep optical trap potentials (100−250 meV), which are able to localize the highly mobile excitons[9] that would otherwise explore large nanotube segments to encounter quenching sites or decay radiatively by E_{11} emission (see Figure 1a).[13] By preventing excitons from reaching quenching sites and decaying nonradiatively, these sp^3 defects can increase the total photoluminescence quantum yield (PLQY) of SWCNTs.[9,14] However, precise control of the degree of sp^3 functionalization is crucial. The maximum ensemble PLQY is observed at fairly low levels of functionalization, which would be favorable for electrically pumped light-emitting devices.[15] In contrast, single-photon emission requires exactly one luminescent defect per SWCNT.[1] Hence, accurate control over the degree of functionalization and knowledge of the precise sp^3 defect densities are highly desired for further optimization.

The emission wavelengths of functionalized SWCNTs are predominantly determined by the binding configuration of the defects, as two sp^2 carbon atoms must be converted to sp^3 carbons to form one defect state. In chiral SWCNTs there are six possible relative positions of the involved carbon atoms, all of which lead to different optical trap depths and photoluminescence (PL) peak wavelengths.[16,17] However, only two of them are commonly found in functionalized (6,5) SWCNTs and give rise to separate NIR emission peaks termed $E_{11}{}^*$ and $E_{11}{}^{*-}$, the latter being more red-shifted and exhibiting a longer fluorescence lifetime than the former.[5,18]

Various synthetic methods have been developed in an attempt to control the degree and type of sp^3 functionalization of nanotube dispersions in water or organic solvents.[14,18−20] However, comparing different reports on functionalized SWCNTs and their properties is difficult because of the use of indirect metrics for their quantification. For example, PL peak intensity ratios strongly depend on the specific experimental setup and excitation power. They only provide a relative but not an absolute defect density.[21] Currently, the most reliable technique to determine the number of luminescent defects on individual SWCNTs is to count distinct emission peaks at cryogenic temperatures.[5,22] However, this method requires substantial experimental effort and tedious statistical analysis.

For graphene, a simple approach to quantify lattice defect densities using Raman spectroscopy is already well-established.[23,24] The introduction of point-like defects into the planar sp^2 carbon lattice leads to the activation of the Raman D mode. Its relative intensity compared to the G mode can be

Received: March 15, 2022
Accepted: April 12, 2022
Published: April 14, 2022

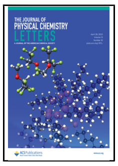

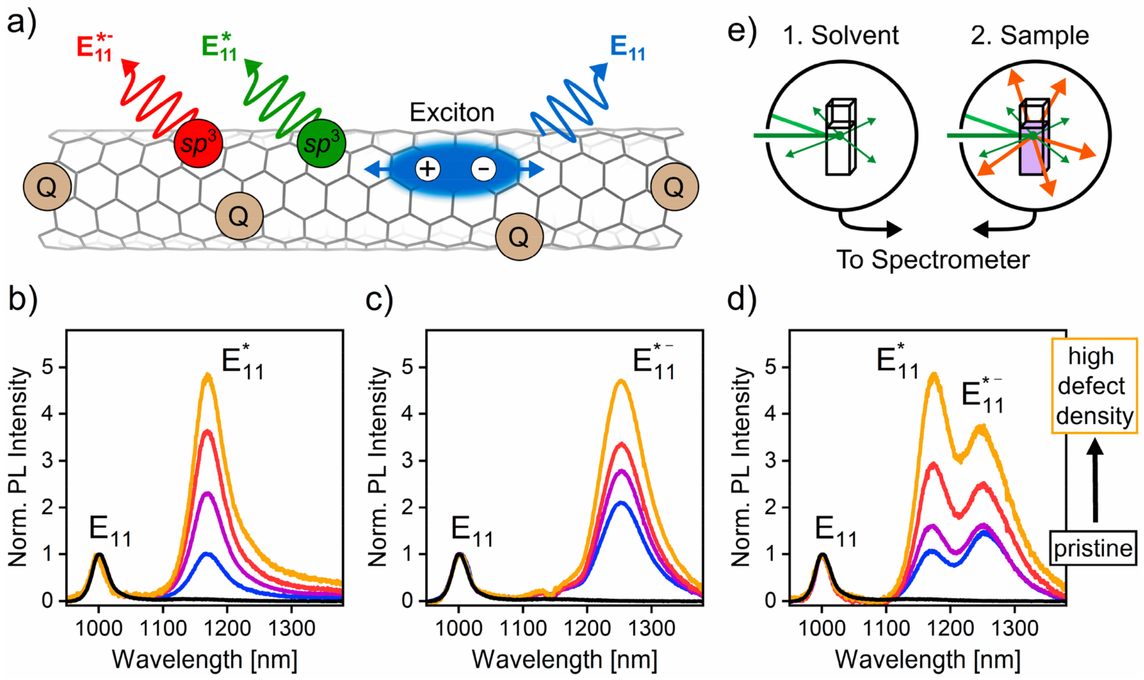

Figure 1. (a) Schematic illustration of a (6,5) SWCNT functionalized with luminescent sp^3 defects. Mobile excitons can decay radiatively (E_{11} emission) or nonradiatively by quenching at nanotube ends and defect sites (Q). Localized sp^3 defects result in red-shifted emission (E_{11}* or E_{11}*$^-$). Normalized (to E_{11}) PL spectra of polymer-sorted (6,5) SWCNTs functionalized (b) with 4-nitrobenzenediazonium tetrafluoroborate (E_{11}* defects), (c) with 2-iodoaniline (E_{11}*$^-$ defects), and (d) with both E_{11}* and E_{11}*$^-$ defects using a sequential reaction scheme. (e) Schematic of absolute PLQY measurements with an integrating sphere.

used as a direct metric for the areal defect density.[25] The corresponding equation has been applied as a means of quality control in graphene samples[26] and to monitor the degree of chemical functionalization.[27] It was recently modified and extended to include line defects in graphene.[28] Although the Raman D mode of SWCNTs also reflects the degree of structural disorder and number of defects,[29−32] no quantitative relation to the absolute density of defects, especially at low defect densities, has been reported so far.

Here, we present a robust empirical metric for the absolute quantification of sp^3 defects in the most commonly used (6,5) SWCNTs. Our method is based on a cross-correlation of Raman spectra, PLQY data, and statistics of low-temperature single-nanotube PL measurements. The final protocol only requires resonant Raman spectroscopy of drop-cast SWCNT films. That way, we are able to extract the absolute sp^3 defect density, independent of type, within an error of ±3 defects per micrometer.

To produce nanotube samples with a controlled number of defects per nanotube length, polymer-sorted (6,5) SWCNTs were functionalized using two different procedures (see Methods, Supporting Information). E_{11}* defects (emission at ∼1170 nm) were introduced by treatment with 4-nitrobenzenediazonium tetrafluoroborate ($DzNO_2$) in a mixture of toluene/acetonitrile employing a phase-transfer agent.[14] More red-shifted E_{11}*$^-$ defects (emission at ∼1250 nm) were created by reaction with 2-iodoaniline in the presence of the organic base potassium *tert*-butoxide (KO^tBu).[18] The degree of sp^3 functionalization was controlled by variation of the $DzNO_2$ concentration or by adjusting the reaction time with 2-iodoaniline. Figure 1b,c shows the corresponding normalized PL spectra of selectively functionalized (6,5) SWCNT dispersions collected under pulsed excitation at the E_{22} transition (575 nm). Furthermore, we employed a sequential reaction scheme to create (6,5) SWCNTs with controlled concentrations of E_{11}* and E_{11}*$^-$ defects as shown in Figure 1d.

The increasing defect emission intensities in relation to the intrinsic E_{11} emission (∼1000 nm) reflect the rising number of defects, but this ratio strongly depends on excitation power[14,18] and cannot provide an absolute number. In contrast to that, absolute PLQY values of functionalized SWCNT dispersions can be used to calculate the density of luminescent sp^3 defects within the framework of the diffusion-limited contact quenching (DLCQ) model. The DLCQ model assumes that excitonic E_{11} emission is governed by exciton diffusion and nonradiative decay at stationary quenching sites.[13] Within this model, luminescent sp^3 defects represent an additional relaxation pathway competing for mobile excitons and resulting in a lower E_{11} PLQY of the functionalized SWCNTs (η^*) compared to pristine SWCNTs (η) as introduced by Miyauchi et al.[10] The ratio (η/η^*) can be used to calculate the density of luminescent defects n_d [μm^{-1}] according to

$$n_{\mathrm{d}} = \sqrt{\frac{\pi}{2\eta D\tau_{\mathrm{rad}}}}\left(\sqrt{\frac{\eta}{\eta^*}} - 1\right) \tag{1}$$

where D is the exciton diffusion constant and τ_{rad} is the radiative lifetime of the E_{11} exciton. The values for D and τ_{rad} were taken from previous experimental studies on (6,5) SWCNTs[13,33] (for details, see the Supporting Information). Absolute PLQY values of SWCNT dispersions can be obtained from the direct measurement of absorbed and emitted photons in an integrating sphere in comparison to a reference sample (cuvette with solvent, see Figure 1e and Supporting Information for experimental details) as described previously.[34]

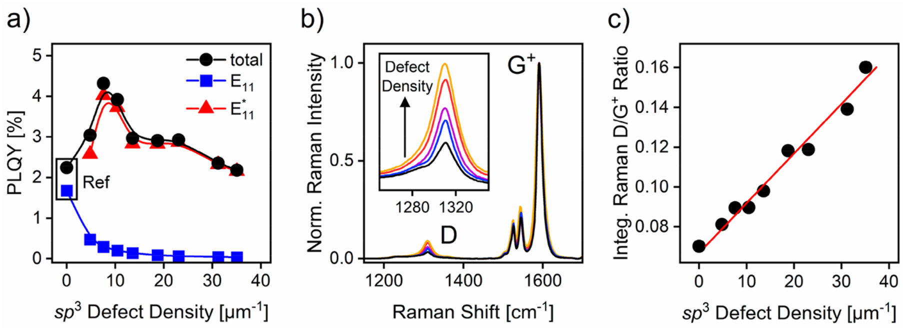

Figure 2. (a) PLQY data with spectral contributions of the E_{11} (without sidebands) and E_{11}* emission at different defect densities for (6,5) SWCNTs functionalized with $DzNO_2$. Lines are guides to the eye. (b) Normalized Raman spectra of sp^3-functionalized (6,5) SWCNTs with a zoom-in on the D mode region as an inset. (c) Correlation of the integrated Raman D/G$^+$ ratio and defect density calculated from E_{11} PLQY with linear fit (red line, R^2 = 0.98).

The spectral contributions of the intrinsic excitonic E_{11} emission and defect emission (E_{11}*, E_{11}*$^-$) are separated, and the defect density is calculated using eq 1 with only the E_{11} PLQY. Based on the uncertainties of the PLQY measurements and the error margins of the reported D and τ_{rad} values, a relative uncertainty of the defect density of about 15% can be estimated. Figure 2a shows the E_{11} and E_{11}* contributions to the total PLQY versus the calculated defect densities for (6,5) SWCNTs functionalized with different concentrations of $DzNO_2$. Pristine (6,5) SWCNTs exhibit a total PLQY of ~2% in dispersion. Low levels of luminescent defects (up to ~10 μm^{-1}) increase the total PLQY by a factor of 2 followed by a strong reduction of the total PL yield at higher degrees of functionalization, in agreement with previous studies.[14,18]

A major drawback of this approach is the necessity of an experimental setup with an integrating sphere for determining the PLQY in combination with precisely defined measurement conditions to prevent distortions due to photon reabsorption.[35] In contrast, determining the relative integrated D mode (I_D, 1200−1400 cm^{-1}) to G$^+$ mode intensity (I_{G^+}, 1560−1640 cm^{-1}) from Raman spectra of the corresponding drop-cast nanotube films is straightforward and very reliable. As shown in Figure 2b, the D mode intensity increases with the degree of functionalization, being indicative of the number of sp^3 carbon atoms. Figure 2c confirms a linear correlation of the integrated Raman signal ratio (I_D/I_{G^+}) with the calculated defect densities obtained from the E_{11} PLQY data in Figure 2a.

The linear correlation in Figure 2c should enable a direct evaluation of the number of sp^3 defects based only on Raman spectra of functionalized (6,5) SWCNTs. However, this metric does not take into account the variations in initial quality of nanotubes before functionalization and thus the variability of the Raman D/G$^+$ ratios of the pristine samples. As sp^3 functionalization adds luminescent defects to a SWCNT lattice that already contains a certain number of defects depending on starting material and processing, the absolute Raman D/G$^+$ ratios cannot be used to determine the number of introduced sp^3 defects. Hence, we propose to use the difference between the integrated Raman D/G$^+$ ratios of the pristine and functionalized sample, i.e., $\Delta(I_D/I_{G^+})$, as a suitable metric for the quantification of defects introduced by functionalization. Note that we use the integrated Raman D/G$^+$ ratio instead of just the peak intensity ratio because it provides more reliable and reproducible values, especially for small changes in defect density.

This differential integrated Raman D/G$^+$ ratio enables comparison between different batches of nanotubes and different functionalization methods. Figure 3 shows a summary of different batches of functionalized (6,5) SWCNTs (see Supporting Information, Figures S1−S3 for detailed PLQY data, PL and Raman spectra). The linear correlation of $\Delta(I_D/I_{G^+})$ with the defect density extracted from the PLQY data holds for different defect densities, various SWCNT batches, E_{11}* and E_{11}*$^-$ defects as well as sequential functionalization to create both defects.

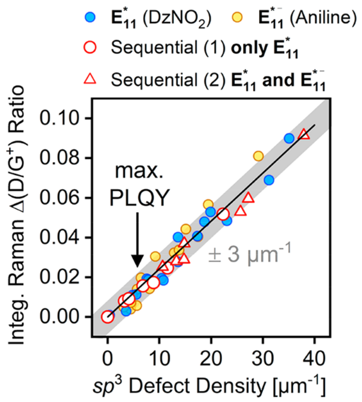

Figure 3. Differential integrated Raman D/G$^+$ ratio versus calculated defect densities for different batches of polymer-wrapped (6,5) SWCNTs with E_{11}*, E_{11}*$^-$ and both defect configurations, including linear fit (black solid line, R^2 = 0.98) and estimated error margin (±3 μm^{-1} shaded in gray). Arrow: defect densities for maximum PLQY (4−8 μm^{-1}).

A linear fit to the compiled data yields the following simple expression for the density of introduced sp^3 defects in (6,5) SWCNTs:

$$n_d = (414 \pm 11)\ \mu\mathrm{m}^{-1} \cdot \Delta\left(\frac{I_D}{I_{G^+}}\right) \tag{2}$$

This equation is valid across a wide range of relevant defect densities (2−40 defects μm^{-1}) and, in particular, covers the defect densities associated with maximum total PLQYs (i.e., 4−8 defects μm^{-1}).

To exclude any potential influence of the laser excitation power on the integrated Raman D/G$^+$ ratios and thus extracted defect densities, Raman spectra of functionalized (6,5) SWCNTs were recorded under identical conditions but at

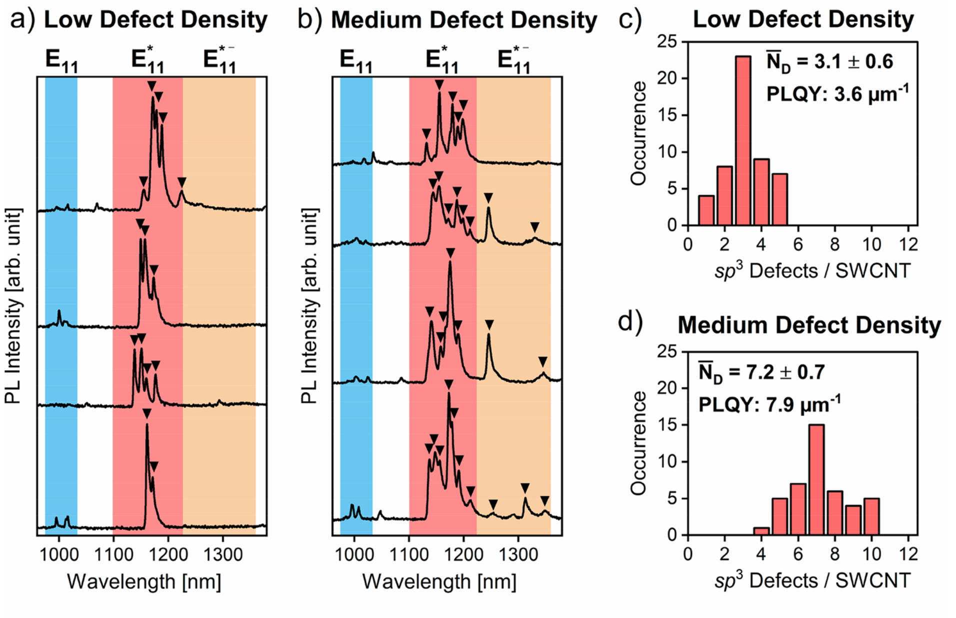

Figure 4. Low-temperature (4.6 K) single-SWCNT PL spectra of (6,5) SWCNTs in a polystyrene matrix functionalized with (a) low and (b) medium defect densities. Black triangles indicate individual defect emission peaks, spectral regions are highlighted for E_{11} (blue), $E_{11}*$ (red), and $E_{11}*^{-}$ (orange) emission. Defect peak histograms of (c) 51 functionalized (6,5) SWCNTs with defect density 3.6 μm^{-1} and (d) 43 functionalized (6,5) SWCNTs with defect density 7.9 μm^{-1} as calculated from PLQY data.

different excitation power densities (see Figure S4, Supporting Information). No significant changes of the integrated Raman D/G^+ ratios were observed. Values obtained at typical laser power densities for Raman spectroscopy of (6,5) SWCNTs should also be comparable between different Raman spectrometers. Thus, this simple metric enables a quick and precise characterization of functionalized SWCNTs, and could be used for a reliable comparison of experiments in different laboratories using different experimental setups. It could also be applied to quickly identify a batch of functionalized nanotubes that is most likely to produce the strongest NIR emission upon excitation.

Note that other possible metrics were also tested, such as the integrated defect-to-E_{11} absorption and emission ratios. In general, absorption ratios are rather unreliable because of the very low absorbance values for $E_{11}*$ and $E_{11}*^{-}$ transitions at low defect densities even for fairly concentrated dispersions (see Figure S5, Supporting Information). No clear correlation with the calculated defect densities could be identified across different SWCNT batches and defect configurations (see Figure S6, Supporting Information). The more commonly employed defect-to-E_{11} emission ratio, which can assess the relative degree of sp^3 functionalization of SWCNTs,[20,36,37] is not applicable across different batches and functionalization methods because of the nonlinear and variable dependence of E_{11} and defect emission on excitation power (see Figure S7, Supporting Information).[18,38]

The demonstrated cross-correlation of integrated Raman D/G^+ ratios and defect densities calculated from E_{11} PLQY data enables a simple evaluation of sp^3 defect densities. However, even the DLCQ model only quantifies the number of defects indirectly and relies heavily on correct values for the exciton diffusion constant and radiative lifetime. In contrast, PL spectra of individual functionalized SWCNTs at cryogenic temperature (cryo-PL) allow for each luminescent defect to be counted as a separate emission peak,[22,39] assuming that each distinguishable peak within the $E_{11}*$ or $E_{11}*^{-}$ spectral emission range corresponds to precisely one sp^3 defect of the respective binding configuration. Different defect emission intensities only reflect the integrated probability for exciton relaxation in a given defect state (not multiple defects), as previously reported for the intrinsic E_{11} transition.[22]

To cross-check the calculated defect densities from PLQY measurements, two samples of (6,5) SWCNTs that were functionalized with low and medium densities of $E_{11}*$ defects (spectral region 1100−1220 nm) were produced and PL spectra at 4.6 K from a large number of individual nanotubes embedded in a polystyrene matrix were statistically analyzed (see Figure 4). At low calculated defect densities of ∼4 μm^{-1}, only few defect emission peaks were found in over 50 representative spectra (see Figures 4a and S8, Supporting Information). At medium defect densities (∼8 μm^{-1}) significantly more defect PL peaks were identified on more than 40 single SWCNTs (see Figures 4b and S9, Supporting Information). Some $E_{11}*^{-}$ defects (spectral region 1220−1360 nm) were found for these defect densities, which is consistent with literature reports for (6,5) SWCNTs functionalized with $DzNO_2$.[16,17,40] As both defect configurations contribute equally to E_{11} quenching within the DLCQ model, and the developed quantification metric does not depend on the binding configuration, all defect peaks were included in the statistical analysis. The respective histograms for the number of defects per nanotube at low and medium sp^3 defect densities are shown in Figure 4c,d. The defect densities calculated from PLQY data and the average defect densities obtained from histograms are in good agreement. However, while calculated defect densities are given per micrometer of SWCNT, cryo-PL spectra show defects on individual nanotubes with unknown length. Hence, the length distribution of sp^3-functionalized SWCNTs needs to be considered for a thorough comparison. For this purpose, atomic force micrographs of nanotubes from the same dispersion of functionalized SWCNTs as those used in cryo-PL spectroscopy were recorded and statistically analyzed (see Figures S8 and S9, Supporting Information). Both pristine and functionalized (6,5) SWCNTs exhibited average lengths of ~1.6 μm. This length distribution suggests that the number of defects per micrometer obtained via cryo-PL measurements is actually slightly lower than that extracted from PLQY measurements (possibly due to a selection bias toward less bright spots to avoid bundles and not all introduced defects being bright, see Supporting Information) but still within the margin of error (±3 μm^{-1}) established in eq 2.

Although eq 2 was derived from measurements of long, polymer-wrapped (6,5) SWCNTs functionalized in organic solvents, the method is also applicable to short nanotubes and aqueous dispersions of SWCNTs. We used $DzNO_2$ to functionalize polymer-sorted (6,5) SWCNTs that were intentionally shortened to average lengths of 0.46 μm by tip sonication (Supporting Information, Figures S10 and S11) and (6,5) SWCNTs sorted by aqueous two-phase extraction (ATPE), stabilized by surfactants in water (see Methods and Figure S12, Supporting Information). For both, a linear correlation between the differential Raman D/G$^+$ ratios and calculated defect densities in agreement with eq 2 was found (see Figure 5a). Moreover, nearly monochiral dispersions of polymer-sorted (7,5) SWCNTs were functionalized with $DzNO_2$ (see Methods and Figure S13, Supporting Information) in a first attempt to expand our approach to other nanotube species. Because of the lower reactivity of (7,5) SWCNTs compared to (6,5) SWCNTs,[18] a maximum absolute defect density of ~20 μm^{-1} was achieved. Nevertheless, the presented quantification method was also applicable to (7,5) SWCNTs (wrapped with polydioctylfluorene, PFO) as shown in Figure 5b, although with some deviations in the precise slope.

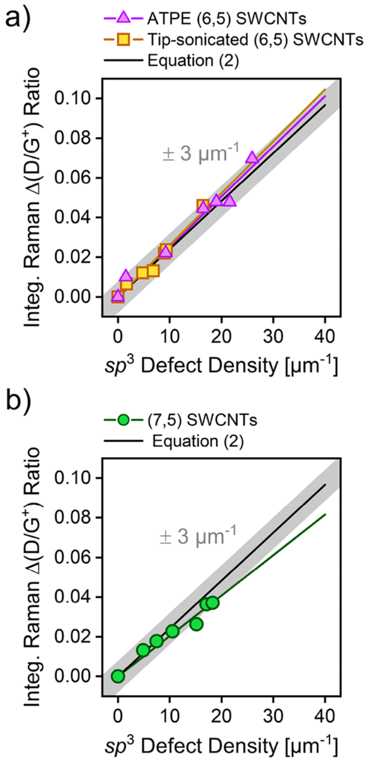

Figure 5. Differential integrated Raman D/G$^+$ ratio versus calculated defect densities and linear fits for (a) aqueous dispersions of ATPE-sorted (6,5) SWCNTs and tip-sonicated, polymer-wrapped (6,5) SWCNTs and for (b) polymer-wrapped (7,5) SWCNTs. All functionalization steps were performed with $DzNO_2$.

This is particularly interesting as resonant Raman measurements of (7,5) SWCNTs are performed at a different excitation wavelength (633 nm) compared to (6,5) SWCNTs (532 nm). For point-like defects in graphene, Cançado et al. reported a strong dependence of the Raman D/G intensity ratio on excitation laser wavelength, which was included in the expression for the average defect distance. However, for large defect distances, the influence of the excitation wavelength on the absolute Raman D/G intensity ratio becomes negligible.[23] The mean defect distances in sp^3-functionalized SWCNTs relevant for most applications and investigated here (20−300 nm, see Figure S14, Supporting Information) are much larger than those considered in studies of defective graphene (5−30 nm).[25] Nevertheless, it remains to be tested what impact the Raman laser excitation wavelength has on SWCNTs with larger diameters.

One direct application of the presented quantification method is the experimental determination of the oscillator strengths of E_{11}* and E_{11}*$^-$ defects. Integration of the defect peak areas in the NIR absorption spectra of functionalized SWCNTs with different defect densities yielded the integrated molar absorptivities and absorption cross sections of the E_{11}* and E_{11}*$^-$ states (see Table 1 and Figure S15, Supporting Information). The oscillator strength of an optical transition was calculated using

Table 1. Integrated Absorptivity, Integrated Absorption Cross Section, and Oscillator Strength per Defect for E_{11}* and E_{11}*$^-$ Defect Configurations, Obtained from NIR Absorption Data of sp^3-Functionalized (6,5) SWCNTs

defect configuration	integrated absorptivity $\int \varepsilon_D d\lambda$ [cm^{-1}nm L mol^{-1}]	integrated absorption cross section $\int \sigma d\tilde{\upsilon}$ [cm]	oscillator strength f
E_{11}^*	(7.8 ± 1.4)·10^7	(3.1 ± 0.5)·10^{-12}	3.5 ± 0.6
E_{11}^{*-}	(2.5 ± 0.4)·10^7	(1.0 ± 0.3)·10^{-12}	1.1 ± 0.3

$$f = \frac{4\varepsilon_0 c^2 m_e \ln(10)}{N_A e^2} \int \varepsilon_D d\tilde{\upsilon} \tag{3}$$

where ε_0 denotes the vacuum permittivity, c is the speed of light, m_e is the electron mass, N_A is Avogadro's number, e is the elementary charge, ε_D is the molar extinction coefficient of the E_{11}* or E_{11}*$^-$ transition, and $\tilde{\upsilon}$ is the wavenumber.[41]

For E_{11}* and E_{11}*$^-$ defects, oscillator strengths of (3.5 ± 0.6) and (1.1 ± 0.3) per defect were obtained, respectively. The error margins for the oscillator strengths of E_{11}* and E_{11}*$^-$ are mainly due to the low total absorbances of the sp^3 defects and the corresponding uncertainties of the integrated defect absorption (see Figure S5, Supporting Information). While density functional theory calculations predicted larger oscillator strengths (by a factor of 3−5),[16,17] they also suggested a reduction of the oscillator strength with a greater red-shift of the defect emission, which is in agreement with our findings. It is important to note that the discussed spectroscopic metrics provided here are given per defect site and are not directly comparable to literature data on the E_{11} oscillator strengths of (6,5) SWCNTs (~0.01 per carbon atom).[42] As electron−hole correlation lengths are still on the order of 1 nm despite localization at defect sites,[43] ~100 carbon atoms are presumed to contribute to the sp^3 defect oscillator strength. Although the acquired data is not accurate enough to corroborate an increase of oscillator strength by a factor of 2 upon exciton trapping as proposed by Miyauchi et al.,[10] our findings suggest that the oscillator strengths of sp^3 defects are at least on the same order of magnitude as those for the E_{11} transition.

In conclusion, we have developed a straightforward and reliable method to quantify the number of sp^3 defects in (6,5) SWCNTs using resonant Raman spectroscopy. By establishing a linear correlation between the differential integrated Raman D/G^+ ratio and sp^3 defect densities calculated from PLQYs, the number of added defects per micrometer nanotube can be obtained within an error margin of ±3 defects μm^{-1}. This method is suitable for SWCNTs functionalized with $E_{11}{}^*$, $E_{11}{}^{*-}$, or both defect configurations, independent of the type of dispersion (polymer-wrapped in organic solvent or surfactant-stabilized in water) and nanotube length of the starting material. A statistical analysis based on PL spectra of individual (6,5) SWCNTs at cryogenic temperature provided direct access to the number of defects per nanotube, which roughly matched the densities calculated from Raman spectra. From these data, the oscillator strengths of the $E_{11}{}^*$ and $E_{11}{}^{*-}$ defects were determined experimentally, confirming the predicted decrease in oscillator strength with optical trap depth of the defects. The applicability of the presented quantification method also extends to other nanotube species as demonstrated for (7,5) SWCNTs. However, additional resonant Raman and PLQY data of functionalized SWCNTs with different diameters will be required to obtain a universal expression similar to that for defects in graphene.

■ ASSOCIATED CONTENT

Supporting Information

The Supporting Information is available free of charge at https://pubs.acs.org/doi/10.1021/acs.jpclett.2c00758.

> Experimental details, characterization methods, calculation of sp^3 defect densities, additional data for functionalized SWCNTs (PLQY; PL, Raman, absorption spectra), Raman laser power density dependence of integrated D/G^+ ratios, low-temperature PL spectra of individual nanotubes, AFM length statistics, calculation of integrated molar absorptivities (PDF)

■ AUTHOR INFORMATION

Corresponding Author

Jana Zaumseil − *Institute for Physical Chemistry, Universität Heidelberg, D-69120 Heidelberg, Germany;* orcid.org/0000-0002-2048-217X; Email: zaumseil@uni-heidelberg.de

Authors

Finn L. Sebastian − *Institute for Physical Chemistry, Universität Heidelberg, D-69120 Heidelberg, Germany;* orcid.org/0000-0003-1161-633X

Nicolas F. Zorn − *Institute for Physical Chemistry, Universität Heidelberg, D-69120 Heidelberg, Germany;* orcid.org/0000-0001-9651-5612

Simon Settele − *Institute for Physical Chemistry, Universität Heidelberg, D-69120 Heidelberg, Germany;* orcid.org/0000-0002-0082-2587

Sebastian Lindenthal − *Institute for Physical Chemistry, Universität Heidelberg, D-69120 Heidelberg, Germany*

Felix J. Berger − *Institute for Physical Chemistry, Universität Heidelberg, D-69120 Heidelberg, Germany;* Present Address: F.J.B.: Center for Nano Science and Technology @PoliMi, Istituto Italiano di Tecnologia, I-20133 Milano, Italy; orcid.org/0000-0003-2834-0050

Christoph Bendel − *Institute for Physical Chemistry, Universität Heidelberg, D-69120 Heidelberg, Germany*

Han Li − *Institute of Nanotechnology, Karlsruhe Institute of Technology, D-76131 Karlsruhe, Germany*

Benjamin S. Flavel − *Institute of Nanotechnology, Karlsruhe Institute of Technology, D-76131 Karlsruhe, Germany;* orcid.org/0000-0002-8213-8673

Complete contact information is available at: https://pubs.acs.org/10.1021/acs.jpclett.2c00758

Notes

The authors declare no competing financial interest.

■ ACKNOWLEDGMENTS

This project has received funding from the European Research Council (ERC) under the European Union's Horizon 2020 research and innovation programme (Grant Agreement No. 817494 "TRIFECTs"). B.S.F. and H.L. acknowledge funding from the Deutsche Forschungsgemeinschaft (DFG) under research grants FL 834/2-2, FL 834/5-1, FL 834/7-1, FL 834/9-1 and FL 834/13-1.

■ REFERENCES

(1) He, X.; Htoon, H.; Doorn, S. K.; Pernice, W. H. P.; Pyatkov, F.; Krupke, R.; Jeantet, A.; Chassagneux, Y.; Voisin, C. Carbon Nanotubes as Emerging Quantum-Light Sources. *Nat. Mater.* **2018**, *17*, 663−670.

(2) Luo, Y.; He, X.; Kim, Y.; Blackburn, J. L.; Doorn, S. K.; Htoon, H.; Strauf, S. Carbon Nanotube Color Centers in Plasmonic Nanocavities: A Path to Photon Indistinguishability at Telecom Bands. *Nano Lett.* **2019**, *19*, 9037−9044.

(3) Zheng, Y.; Kim, Y.; Jones, A. C.; Olinger, G.; Bittner, E. R.; Bachilo, S. M.; Doorn, S. K.; Weisman, R. B.; Piryatinski, A.; Htoon, H. Quantum Light Emission from Coupled Defect States in DNA-Functionalized Carbon Nanotubes. *ACS Nano* **2021**, *15*, 10406−10414.

(4) Mandal, A. K.; Wu, X.; Ferreira, J. S.; Kim, M.; Powell, L. R.; Kwon, H.; Groc, L.; Wang, Y.; Cognet, L. Fluorescent sp^3 Defect-Tailored Carbon Nanotubes Enable NIR-II Single Particle Imaging in Live Brain Slices at Ultra-Low Excitation Doses. *Sci. Rep.* **2020**, *10*, 5286.

(5) Berger, F. J.; de Sousa, J. A.; Zhao, S.; Zorn, N. F.; El Yumin, A. A.; Quintana Garcia, A.; Settele, S.; Högele, A.; Crivillers, N.; Zaumseil, J. Interaction of Luminescent Defects in Carbon Nanotubes with Covalently Attached Stable Organic Radicals. *ACS Nano* **2021**, *15*, 5147−5157.

(6) Spreinat, A.; Dohmen, M. M.; Lüttgens, J.; Herrmann, N.; Klepzig, L. F.; Nißler, R.; Weber, S.; Mann, F. A.; Lauth, J.; Kruss, S. Quantum Defects in Fluorescent Carbon Nanotubes for Sensing and Mechanistic Studies. *J. Phys. Chem. C* **2021**, *125*, 18341−18351.

(7) Zaumseil, J. Luminescent Defects in Single-Walled Carbon Nanotubes for Applications. *Adv. Optical Mater.* **2022**, *10*, 2101576.

(8) Ghosh, S.; Bachilo, S. M.; Simonette, R. A.; Beckingham, K. M.; Weisman, R. B. Oxygen Doping Modifies Near-Infrared Band Gaps in Fluorescent Single-Walled Carbon Nanotubes. *Science* **2010**, *330*, 1656−1659.

(9) Piao, Y.; Meany, B.; Powell, L. R.; Valley, N.; Kwon, H.; Schatz, G. C.; Wang, Y. Brightening of Carbon Nanotube Photoluminescence

through the Incorporation of sp^3 Defects. *Nat. Chem.* **2013**, *5*, 840−845.

(10) Miyauchi, Y.; Iwamura, M.; Mouri, S.; Kawazoe, T.; Ohtsu, M.; Matsuda, K. Brightening of Excitons in Carbon Nanotubes on Dimensionality Modification. *Nat. Photonics* **2013**, *7*, 715−719.

(11) Shiraki, T.; Miyauchi, Y.; Matsuda, K.; Nakashima, N. Carbon Nanotube Photoluminescence Modulation by Local Chemical and Supramolecular Chemical Functionalization. *Acc. Chem. Res.* **2020**, *53*, 1846−1859.

(12) Brozena, A. H.; Kim, M.; Powell, L. R.; Wang, Y. Controlling the Optical Properties of Carbon Nanotubes with Organic Colour-Centre Quantum Defects. *Nat. Rev. Chem.* **2019**, *3*, 375−392.

(13) Hertel, T.; Himmelein, S.; Ackermann, T.; Stich, D.; Crochet, J. Diffusion Limited Photoluminescence Quantum Yields in 1-D Semiconductors: Single-Wall Carbon Nanotubes. *ACS Nano* **2010**, *4*, 7161−7168.

(14) Berger, F. J.; et al. Brightening of Long, Polymer-Wrapped Carbon Nanotubes by sp^3 Functionalization in Organic Solvents. *ACS Nano* **2019**, *13*, 9259−9269.

(15) Zorn, N. F.; Berger, F. J.; Zaumseil, J. Charge Transport in and Electroluminescence from sp^3-Functionalized Carbon Nanotube Networks. *ACS Nano* **2021**, *15*, 10451−10463.

(16) Gifford, B. J.; Kilina, S.; Htoon, H.; Doorn, S. K.; Tretiak, S. Exciton Localization and Optical Emission in Aryl-Functionalized Carbon Nanotubes. *J. Phys. Chem. C* **2018**, *122*, 1828−1838.

(17) Saha, A.; Gifford, B. J.; He, X.; Ao, G.; Zheng, M.; Kataura, H.; Htoon, H.; Kilina, S.; Tretiak, S.; Doorn, S. K. Narrow-Band Single-Photon Emission through Selective Aryl Functionalization of Zigzag Carbon Nanotubes. *Nat. Chem.* **2018**, *10*, 1089−1095.

(18) Settele, S.; Berger, F. J.; Lindenthal, S.; Zhao, S.; El Yumin, A. A.; Zorn, N. F.; Asyuda, A.; Zharnikov, M.; Högele, A.; Zaumseil, J. Synthetic Control over the Binding Configuration of Luminescent sp^3-Defects in Single-Walled Carbon Nanotubes. *Nat. Commun.* **2021**, *12*, 2119.

(19) Kwon, H.; Furmanchuk, A.; Kim, M.; Meany, B.; Guo, Y.; Schatz, G. C.; Wang, Y. Molecularly Tunable Fluorescent Quantum Defects. *J. Am. Chem. Soc.* **2016**, *138*, 6878−6885.

(20) Zheng, Y.; Bachilo, S. M.; Weisman, R. B. Photoexcited Aromatic Reactants Give Multicolor Carbon Nanotube Fluorescence from Quantum Defects. *ACS Nano* **2020**, *14*, 715−723.

(21) Iwamura, M.; Akizuki, N.; Miyauchi, Y.; Mouri, S.; Shaver, J.; Gao, Z.; Cognet, L.; Lounis, B.; Matsuda, K. Nonlinear Photoluminescence Spectroscopy of Carbon Nanotubes with Localized Exciton States. *ACS Nano* **2014**, *8*, 11254−11260.

(22) Raynaud, C.; Claude, T.; Borel, A.; Amara, M. R.; Graf, A.; Zaumseil, J.; Lauret, J. S.; Chassagneux, Y.; Voisin, C. Superlocalization of Excitons in Carbon Nanotubes at Cryogenic Temperature. *Nano Lett.* **2019**, *19*, 7210−7216.

(23) Cançado, L. G.; Jorio, A.; Ferreira, E. H.; Stavale, F.; Achete, C. A.; Capaz, R. B.; Moutinho, M. V.; Lombardo, A.; Kulmala, T. S.; Ferrari, A. C. Quantifying Defects in Graphene *via* Raman Spectroscopy at Different Excitation Energies. *Nano Lett.* **2011**, *11*, 3190−3196.

(24) Lucchese, M. M.; Stavale, F.; Ferreira, E. H. M.; Vilani, C.; Moutinho, M. V. O.; Capaz, R. B.; Achete, C. A.; Jorio, A. Quantifying Ion-Induced Defects and Raman Relaxation Length in Graphene. *Carbon* **2010**, *48*, 1592−1597.

(25) Beams, R.; Cançado, L. G.; Novotny, L. Raman Characterization of Defects and Dopants in Graphene. *J. Phys.: Condens. Matter* **2015**, *27*, 083002.

(26) Grimm, S.; Schweiger, M.; Eigler, S.; Zaumseil, J. High-Quality Reduced Graphene Oxide by CVD-Assisted Annealing. *J. Phys. Chem. C* **2016**, *120*, 3036−3041.

(27) Englert, J. M.; Vecera, P.; Knirsch, K. C.; Schäfer, R. A.; Hauke, F.; Hirsch, A. Scanning-Raman-Microscopy for the Statistical Analysis of Covalently Functionalized Graphene. *ACS Nano* **2013**, *7*, 5472−5482.

(28) Cançado, L. G.; Gomes da Silva, M.; Martins Ferreira, E. H.; Hof, F.; Kampioti, K.; Huang, K.; Pénicaud, A.; Achete, C. A.; Capaz, R. B.; Jorio, A. Disentangling Contributions of Point and Line Defects in the Raman Spectra of Graphene-Related Materials. *2D Mater.* **2017**, *4*, 025039.

(29) Wang, J.; Shea, M. J.; Flach, J. T.; McDonough, T. J.; Way, A. J.; Zanni, M. T.; Arnold, M. S. Role of Defects as Exciton Quenching Sites in Carbon Nanotube Photovoltaics. *J. Phys. Chem. C* **2017**, *121*, 8310−8318.

(30) Dresselhaus, M. S.; Jorio, A.; Souza Filho, A. G.; Saito, R. Defect Characterization in Graphene and Carbon Nanotubes Using Raman Spectroscopy. *Philos. Trans. R. Soc. A* **2010**, *368*, 5355−5377.

(31) Kalbacova, J.; Garratt, E.; Rodriguez, R. D.; Hight Walker, A. R.; Twedt, K. A.; Fagan, J. A.; Madeira, T. I.; McClelland, J. J.; Nikoobakht, B.; Zahn, D. R. T. Defect Evolution of Ion-Exposed Single-Wall Carbon Nanotubes. *J. Phys. Chem. C* **2019**, *123*, 2496−2505.

(32) Ghosh, S.; Wei, F.; Bachilo, S. M.; Hauge, R. H.; Billups, W. E.; Weisman, R. B. Structure-Dependent Thermal Defunctionalization of Single-Walled Carbon Nanotubes. *ACS Nano* **2015**, *9*, 6324−6332.

(33) Hofmann, M. S.; Gluckert, J. T.; Noe, J.; Bourjau, C.; Dehmel, R.; Högele, A. Bright, Long-Lived and Coherent Excitons in Carbon Nanotube Quantum Dots. *Nat. Nanotechnol.* **2013**, *8*, 502−505.

(34) Graf, A.; Zakharko, Y.; Schießl, S. P.; Backes, C.; Pfohl, M.; Flavel, B. S.; Zaumseil, J. Large Scale, Selective Dispersion of Long Single-Walled Carbon Nanotubes with High Photoluminescence Quantum Yield by Shear Force Mixing. *Carbon* **2016**, *105*, 593−599.

(35) Wei, X.; et al. Photoluminescence Quantum Yield of Single-Wall Carbon Nanotubes Corrected for the Photon Reabsorption Effect. *Nano Lett.* **2020**, *20*, 410−417.

(36) Hartmann, N. F.; Velizhanin, K. A.; Haroz, E. H.; Kim, M.; Ma, X.; Wang, Y.; Htoon, H.; Doorn, S. K. Photoluminescence Dynamics of Aryl sp^3 Defect States in Single-Walled Carbon Nanotubes. *ACS Nano* **2016**, *10*, 8355−8365.

(37) Kim, M.; et al. Fluorescent Carbon Nanotube Defects Manifest Substantial Vibrational Reorganization. *J. Phys. Chem. C* **2016**, *120*, 11268−11276.

(38) Ma, X.; Adamska, L.; Yamaguchi, H.; Yalcin, S. E.; Tretiak, S.; Doorn, S. K.; Htoon, H. Electronic Structure and Chemical Nature of Oxygen Dopant States in Carbon Nanotubes. *ACS Nano* **2014**, *8*, 10782−10789.

(39) Hofmann, M. S.; Noe, J.; Kneer, A.; Crochet, J. J.; Högele, A. Ubiquity of Exciton Localization in Cryogenic Carbon Nanotubes. *Nano Lett.* **2016**, *16*, 2958−2962.

(40) Shiraki, T.; Shiraishi, T.; Juhasz, G.; Nakashima, N. Emergence of New Red-Shifted Carbon Nanotube Photoluminescence Based on Proximal Doped-Site Design. *Sci. Rep.* **2016**, *6*, 28393.

(41) Schöppler, F.; Mann, C.; Hain, T. C.; Neubauer, F. M.; Privitera, G.; Bonaccorso, F.; Chu, D.; Ferrari, A. C.; Hertel, T. Molar Extinction Coefficient of Single-Wall Carbon Nanotubes. *J. Phys. Chem. C* **2011**, *115*, 14682−14686.

(42) Streit, J. K.; Bachilo, S. M.; Ghosh, S.; Lin, C.-W.; Weisman, R. B. Directly Measured Optical Absorption Cross Sections for Structure-Selected Single-Walled Carbon Nanotubes. *Nano Lett.* **2014**, *14*, 1530−1536.

(43) Gifford, B. J.; Kilina, S.; Htoon, H.; Doorn, S. K.; Tretiak, S. Controlling Defect-State Photophysics in Covalently Functionalized Single-Walled Carbon Nanotubes. *Acc. Chem. Res.* **2020**, *53*, 1791−1801.